JOURNAL OF GEOPHYSICAL RESEARCH, VOL. 111, B05305, doi:10.1029/2004JB003270, 2006

Shear velocity variation within the D″ region beneath the central Pacific

Megan Avants,[1] Thorne Lay,[2] Sara A. Russell,[3,4,5] and Edward J. Garnero[6]

Received 28 June 2004; revised 11 January 2006; accepted 24 January 2006; published 4 May 2006.

[1] Small-scale variability of shear velocity (V_s) structure in the D″ region beneath the central Pacific is imaged using 442 broadband tangential component *S* waveforms recorded in western North America for 37 intermediate and deep focus Tonga-Fiji earthquakes. Double-array stacking of spatially binned subsets of data reveals lateral variations in the relative timing and amplitude of deep mantle discontinuity reflections on scale lengths of about 130 km across the $\sim 6° \times 8°$ region of D″ sampled. Waveform modeling using localized one-dimensional structures indicates variations of the V_s increase at the D″ discontinuity ranging from 0.5% to 2.3%, and discontinuity depths ranging from 2490 to 2735 km, deepening and weakening from southwest-to-northeast across the study area. Two abrupt V_s reductions are also detected within the D″ layer. We thus present a laterally variable three-layer model of the D″ region beneath the central Pacific. The complex structure may be associated with lateral thermal and chemical gradients that produce a lens of postperovskite material above an ultralow-velocity zone on the margin of a large low shear velocity province.

Citation: Avants, M., T. Lay, S. A. Russell, and E. J. Garnero (2006), Shear velocity variation within the D″ region beneath the central Pacific, *J. Geophys. Res.*, *111*, B05305, doi:10.1029/2004JB003270.

1. Introduction

[2] The lowermost ~250 km of the mantle, the D″ region, is associated with anomalously low gradients in seismic velocities and increased lateral velocity heterogeneity relative to the overlying mantle [e.g., *Lay et al.*, 2004b]. Global tomography models of the lower mantle consistently indicate large-scale shear velocity (V_s) heterogeneity in D″, with relatively low V_s beneath the central Pacific and southern Atlantic, and relatively high V_s beneath circum-Pacific regions [e.g., *Mégnin and Romanowicz*, 2000; *Ritsema and van Heijst*, 2000; *Grand*, 2002]. Many studies report abrupt V_s and V_p increases near the top of D″, about 100 to 300 km above the core-mantle boundary (CMB) (see review by *Wysession et al.* [1998]). This so-called D″ discontinuity has velocity increases ranging from 0.5 to 3% and may involve a sharp jump or a 30–50 km wide transition zone. Triplication arrivals from the D″ discontinuity are strongest in regions of relatively high V_s in the deep mantle, and are not always clearly observed in other regions. Various interpretations of the D″ discontinuity have been proposed (see review by *Lay and Garnero* [2004]), with the strongest candidate being a phase transition from perovskite to postperovskite [*Murakami et al.*, 2004; *Iitaka et al.*, 2004; *Oganov and Ono*, 2004]. At greater depths, some regions show evidence for an ultralow-velocity zone (ULVZ), which is a thin (5 to 40 km thick) layer at the base of the mantle with very strong reductions of V_s (10% to 30% with respect to PREM [*Dziewonski and Anderson*, 1981]) and *P* velocity (V_p) [e.g., *Thorne and Garnero*, 2004].

[3] The D″ velocity structure beneath the central Pacific Ocean, the focus of this study, has broad regions of low V_s imaged by mantle tomography models and by studies of diffracted waves; model M1 [*Ritsema et al.*, 1997] in Figure 1 is representative of the latter. The large low shear velocity province under the central Pacific appears to have strong lateral gradients on its southern margin [*To et al.*, 2005; *Ford et al.*, 2006], as is also the case for the margins of the low-velocity region under the southern Atlantic [*Wang and Wen*, 2004; *Ni et al.*, 2005]. We study in detail a region on the northern margin of the central Pacific low shear velocity province. A ULVZ has also been reported for this region, characterized primarily by *PcP* precursors [*Mori and Helmberger*, 1995; *Revenaugh and Meyer*, 1997; *Reasoner and Revenaugh*, 1999; *Russell et al.*, 2001]. We add constraints from *ScS* precursors in this study, which provides direct sensitivity to V_s structure.

[4] There have been conflicting interpretations of whether there is a D″ discontinuity in the low-velocity region under the central Pacific [e.g., *Schlittenhardt et al.*, 1985; *Garnero et al.*, 1988, 1993; *Kohler et al.*, 1997; *Reasoner and Revenaugh*, 1999; *Sidorin et al.*, 1999a, 1999b; *Russell et*

[1]Earth Sciences Department, University of California, Santa Cruz, California, USA.
[2]Institute of Geophysics and Planetary Physics, University of California, Santa Cruz, California, USA.
[3]Weston Geophysical Corporation, Lexington, Massachusetts, USA.
[4]Now at Marston Science Library, University of Florida, Gainesville, Florida, USA.
[5]Now Sara Russell Gonzalez.
[6]Department of Geological Sciences, Arizona State University, Tempe, Arizona, USA.

0148-0227/06/2004JB003270$09.00

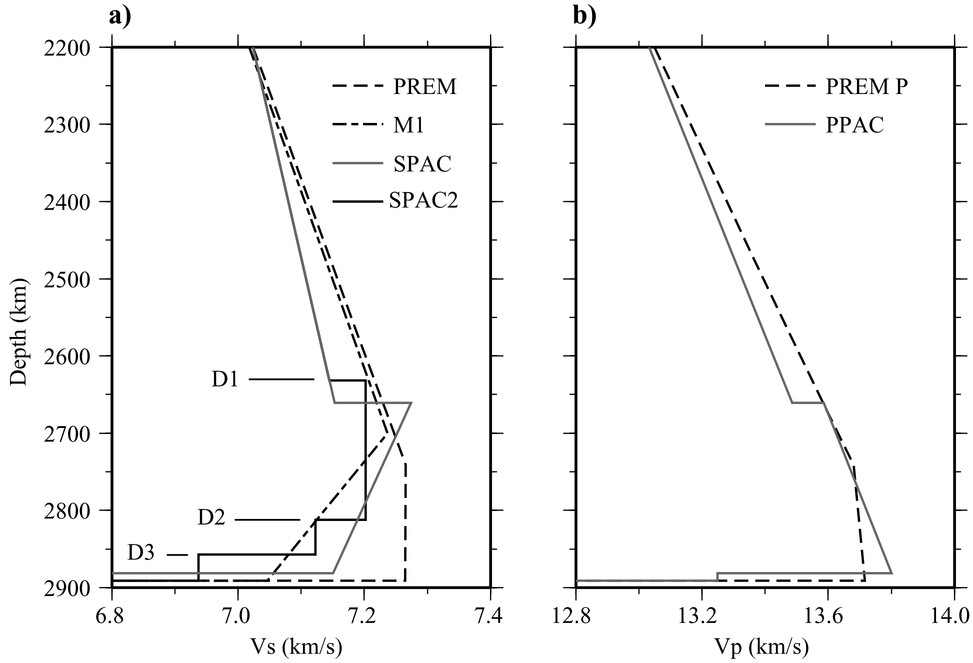

Figure 1. (a) Shear velocity models PREM [*Dziewonski and Anderson*, 1981], M1 [*Ritsema et al.*, 1997], SPAC [*Russell et al.*, 2001], and SPAC2, this study. (b) Compressional velocity models PREM and PPAC [*Russell et al.*, 2001]. Models SPAC and PPAC are discontinuity models previously obtained for our study area under the central Pacific by stacking data distributed over part of the region. We use model M1 as a reference structure for the shear wave stacking in this paper, as it provides a good match to the average *ScS*-*S* observations for the region. SPAC2 models the composite stack of our entire data set (see Figure 4) and is our average model for this region.

al., 2001]. Triplication arrivals from any D″ discontinuity in this region appear to be rather weak and variable, and waveform stacking is needed for reliable detections. *Russell et al.* [2001] stacked *P* and *S* waves sampling a common region, and modeled features in the stacks with V_p and V_s velocity discontinuities 230 km above the CMB. The jumps in V_p and V_s in their models PPAC and SPAC (Figure 1) are somewhat weaker (0.75% and 1.7%, respectively) than usually found in circum-Pacific regions. These models contain a D″ discontinuity and a ULVZ. The central Pacific study region is located in a large-scale southwest-to-northeast gradient from low to moderately high shear velocity (Figure 2b) [e.g., *Garnero and Helmberger*, 1993; *Bréger and Romanowicz*, 1998; *Bréger et al.*, 2001], with negative radial shear velocity gradients across D″ over an extensive area [*Ritsema et al.*, 1997]. This region also straddles the margin of a bulk sound velocity anomaly under the southern central Pacific [*Masters et al.*, 2000; *Lay et al.*, 2004b]; very strong lateral boundaries of the central Pacific low shear velocity structure may be present [e.g., *Luo et al.*, 2001]. In this study, we further characterize the D″ shear velocity structure beneath the central Pacific by waveform stacking and modeling, incorporating significantly more data and deep mantle reflections than previous studies.

2. Data and Methods

[5] Seismic waves from earthquakes in the Tonga-Fiji region recorded by broadband seismic stations in western North America (Figure 2a) comprise our data set. We collect a large data set involving closely spaced stations to enable waveform stacking procedures that can improve the signal-to-noise ratio for any weak lower mantle reflections. We obtained broadband data from stations of the Berkeley Digital Seismic Network (BDSN), Terrascope/TRInet, and IRIS GSN stations in the western U.S. for 64 events in the Tonga-Fiji region between 1990 and 2001 with source depths greater than 100 km and seismic magnitudes ranging from 5.1 to 7.6.

[6] The data span epicentral distances of 74°–85°, an appropriate distance range for observing any lower mantle triplication from a D″ discontinuity [*Lay and Helmberger*, 1983a], with individual events typically having up to a 4° epicentral distance range for our ray path geometry (Figure 2). The number of observations per event varies systematically with date, from as few as 3 for events in 1990 to more than 50 for events in 2001, as broadband networks expanded. Transversely polarized component (*SH*) recordings are used, for the time interval from direct *S*, which turns in the midmantle well above D″, through the core reflection *ScS* (Figure 2b). For our distance range, anomalous D″ shear velocity layering can produce precursors to *ScS*, sampling an area above the CMB of approximately 6° × 8° (Figure 2a). We do not consider the vertically polarized component (*SV*) because the seismogram interval between *S* and *ScS* tends to be complicated by additional arrivals resulting from *SV*-to-*P* conversions, SP_L reverberations beneath the receiver, and by *SKS* arrivals which traverse the core.

[7] Horizontal components are deconvolved by their instrument responses to obtain ground displacement at the

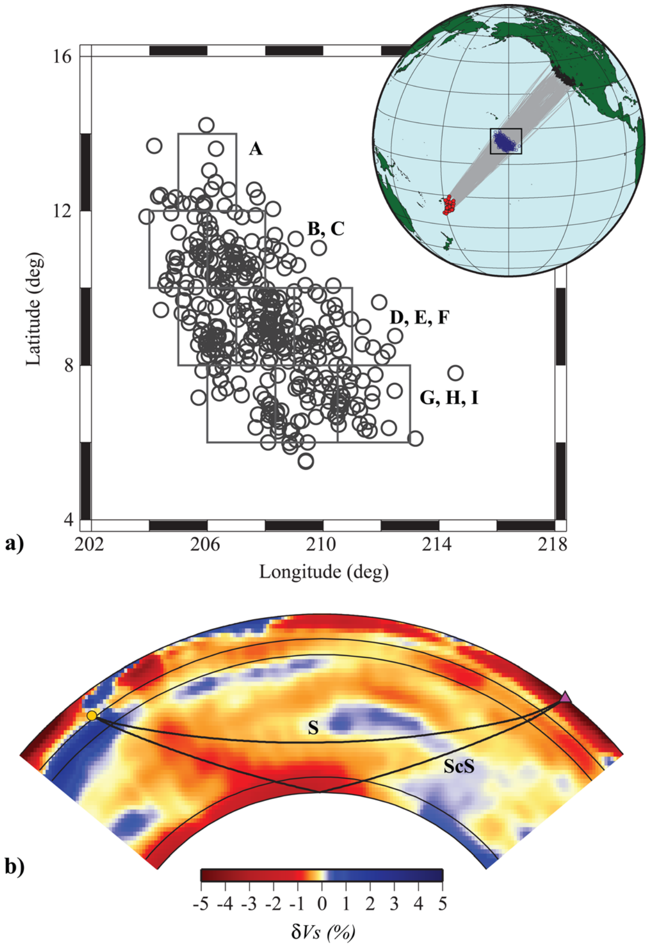

Figure 2. (a) *ScS* bounce points (rings) overlain by the location of nine nonoverlapping subsets of data within our study region. Inset globe shows locations of earthquakes in the Tonga-Fiji region (red circles), *ScS* bounce points beneath the central Pacific (blue circles), and broadband BDSN and TERRAscope/TRInet stations in western North America (black triangles) used in this study. (b) Sample *S* and *ScS* ray paths from our data set superimposed on a shear velocity model cross section [*Grand*, 2002] along the source-receiver great circle plane. Note the very low shear velocities traversed by *ScS* in the lowermost few hundred kilometers of the mantle.

receivers. We then apply corrections for published lithospheric anisotropy characterizations [*Silver*, 1996; *Polet and Kanamori*, 2002] to ensure that our subsequent rotations to the great circle reference frame are not affected by complications from shallow anisotropy. The lithospheric corrections, primarily based on *SKS* data from events at larger distances along the Tonga arc, assume a constant correction for the entire wave train, ignoring any minor dependence on ray parameter. These corrections actually have only minor affects on the tangential component waveforms of our data set. The rotated *SH* displacement records are high-pass filtered using a two-pass Butterworth filter with cutoff frequencies ranging from 0.005 Hz to 0.01–0.02 Hz, depending on the signal quality. This filtering causes a minor baseline shift toward negative amplitudes in our waveform stacks. After rejecting low-quality displacement signals, our data set contained 766 traces from 44 events.

[8] We normalize the remaining traces relative to each *ScS* peak amplitude, and all signals from each event are aligned on the *ScS* phase. We linearly stack the simplest and clearest *ScS* arrivals for each event to produce a reference source wavelet for that event. We crop the *ScS* arrival to be a simple positive pulse free of any immediate precursors from ULVZ reflections and with limited coda. This gives a simple source pulse characteristic of the rupture duration and complexity of the event. Most sources are single pulses, but a few are double pulses or more complex in shape (Figure 3). We then deconvolve the source wavelet from all traces for that event using a water level deconvolution, using minor variations in water level (0.0001 for 38 of the events and up to 0.01 for the largest events) to accommodate signal-to-noise variations. After deconvolution, a low-pass Butterworth filter with a corner frequency of 0.3 Hz is applied to each trace. This yields a slightly filtered spike train of arrivals for each waveform with comparable signal shape and bandwidth between all events.

[9] The *ScS* arrival was used as the reference phase for estimating the source wavelet because it is generally an isolated and clear arrival, and we obtained more stable deconvolutions than if we obtain the stack using direct *S*, which tends to be broader and more variable. This may stem from more tightly bundled rays emerging from the source that produce the *ScS* pulses, as well as from greater validity of the receiver anisotropy correction for the more steeply incident *ScS* arrivals. Figure 3 shows some representative displacements traces and deconvolutions for two events. In the displacement traces *S* and *ScS* are distinct arrivals, but the source time function can obscure any coherent energy between them. Note that for the 13 April 1999 event, the first pulse is significantly wider at ORV than at SAO, and deconvolution isolates the secondary arrival (Scd) in the ORV waveform. After source wavelet deconvolution the data have simpler waveforms with improved temporal resolution due to the bandwidth extension, and data from different events can now be merged in waveform stacking methods that will enhance the signal-to-noise for any weak arrivals with specific slowness relative to *ScS*. Several distance profiles of deconvolved signals are shown in the auxiliary material.[1]

[10] The main challenge in the source wavelet deconvolution processing is that imperfections in the estimated source wavelet and the nature of deconvolution itself result in enhanced high-frequency noise and, in a few cases, ringing of the deconvolution due to misfit of the S waveform by the stacked ScS wavelet. This latter is not always eliminated by the low-pass filter. We visually examine each trace after source wavelet deconvolution and filtering, grading each according to its noise level. The traces for which *ScS* is poorly defined (i.e., not 'spiked up') are removed from the data set; this tends to eliminate events with less favorable radiation patterns for downgoing *SH* energy. Traces with excessive ringing due to misfit of S are also removed. We realign and renormalize on the *ScS* amplitude, obtaining our final data set of 442 traces from

[1]Auxiliary material is available at ftp://ftp.agu.org/apend/jb/2004jb003270.

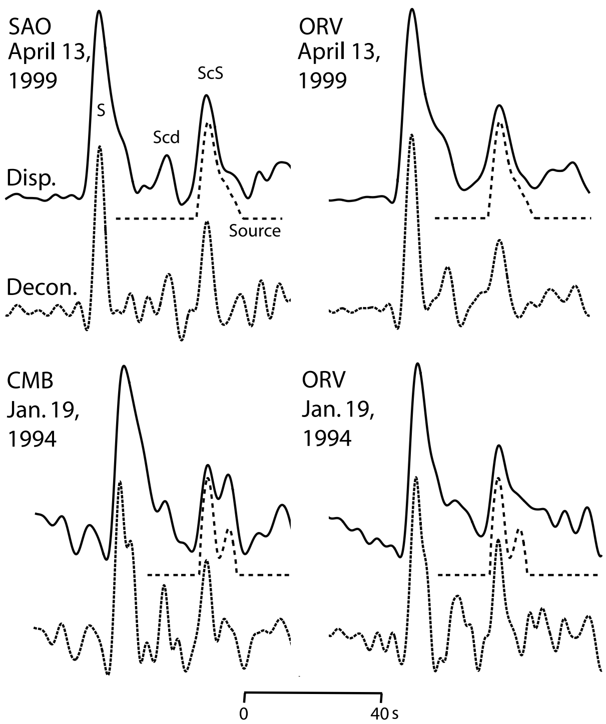

Figure 3. Representative examples of the source wavelet deconvolution procedure. The top row shows two observed *SH* displacement (Disp.) waveforms for the event of 13 April 1999, from stations SAO and ORV. This was a relatively large, m_b = 6.8 event. The estimated source time function obtained by stacking 42 aligned *ScS* waveforms for this event and cropping the stacked signal to give a short one-sided wavelet is shown below the *ScS* waveform for each station (Source). The deconvolutions (Decon.) obtained using a water level of 0.0001 and a two-pass Butterworth low-pass filter with a corner frequency of 0.3 Hz are shown below each trace. The lower row shows similar comparisons of displacements and deconvolutions for the 19 January 1994 event (m_b = 6.1) event for stations CMB and ORV. The latter event is smaller so the signal-to-noise ratio is lower and the source wavelet, estimated by stacking four clear observations (not including these stations), is more impulsive. Deconvolution spikes up the pulses, reducing overlap caused by the source duration, but with some enhancement of short-period noise throughout the signal.

37 events (listed in auxiliary material). The total number of *SH* seismograms sampling our study area is increased by about an order of magnitude from the data set used by *Russell et al.* [2001].

[11] We utilize a double-array stacking algorithm developed by *Revenaugh and Meyer* [1997]. This method computes the move out times relative to a reference phase for a top-side precritical reflection from a target depth in a one-dimensional (1-D) reference velocity structure for a suite of events and receivers. The *ScS* reference phase provides a direct time reference tied to the CMB, and any precursory energy reflecting from overlying D″ layering has source radiation and mantle path attenuation similar to *ScS*. All seismograms are individually time shifted and summed, and the amplitude of the stack at the corresponding alignment is plotted as a function of target depth relative to the reference phase. With our traces aligned and normalized on *ScS*, the double-array stack always has a peak amplitude of 1.0 at the reference depth of the CMB, and reflection amplitudes at other depths are relative to this. The shear velocity at the base of the mantle is extended downward into the core model to provide stacking velocities for depths greater than the CMB, effectively capturing energy after the *ScS* peak amplitude.

[12] Regional shear velocity model M1 (Figure 1), developed by *Ritsema et al.* [1997], is chosen as our reference velocity model for the stacking algorithm because it has been shown to provide a better baseline fit to central Pacific *ScS-S* differential time anomalies than standard Earth models [*Russell et al.*, 1999]. The double-array stacking method explicitly assumes that any *ScS* precursors can be represented as precritical reflections, generically labeled *SdS*, originating from reflector depth, *d*. For the wide-angle, grazing geometry of our data, actual interactions with a high-velocity discontinuity are somewhat more complicated, and involve a triplication of the wavefield with some energy diving below and some reflecting off of the velocity increase [*Lay and Helmberger*, 1983a]. Any associated blurring effects on the stacks can be simulated by processing synthetic waveforms for a discontinuity model through the same algorithm. Because *ScS* geometric spreading causes it to vary in amplitude with distance [e.g., *Lay and Helmberger*, 1983b], normalization on *ScS* requires attention to modeling data with synthetics at corresponding distances.

[13] To provide a comparison with the earlier results of *Russell et al.* [2001], we double-array stack our entire data set (Figure 4), finding a very well defined *ScS* peak at the CMB, a slight negative pulse (D_3) at ~40 km above the CMB, an additional weak negative pulse (D_2) peaking at ~80 km above the CMB, and a rather broad positive feature (D_1) from ~200 to 350 km above the CMB.

[14] Stacking 1-D reflectivity synthetics [e.g., *Müller*, 1985] for model SPAC of *Russell et al.* [2001] (Figure 1a) using the same processing and reference model as for the data, yields the predicted curve in Figure 4 (gray line). Small oscillations in the data stack at depths below the CMB indicate the level of sidelobe oscillations generated by the signal processing as well as some possible *ScS* post-cursor energy (multiple reflections in the ULVZ). Note that the overall baseline of the stack is shifted slightly negative; this is the consequence of the high-pass filtering during the ground displacement restitution. The negative energy just above the CMB corresponds to reflection from the strong shear velocity decrease in a 10 km thick ULVZ. Model SPAC has a 12% V_s reduction, which was scaled by a 3:1 ratio from the 4% V_p reduction obtained by modeling *PcP* precursors. This predicts a stronger negative arrival closer to the CMB than observed, and does not predict the observed feature 80 km above the CMB. The positive discontinuity in SPAC predicts an arrival imaged at ~230 km above the CMB. While SPAC provided a good fit to the sparser data stack of *Russell et al.* [2001], the predicted arrival is narrower and higher amplitude than the broad, low-amplitude data peak in our expanded data stack. We attribute this to variable timing of the reflected arrival for our larger data set, which could be caused by strong lateral variability of the discontinuity depth and/or variations of the velocity structure below the discontinuity.

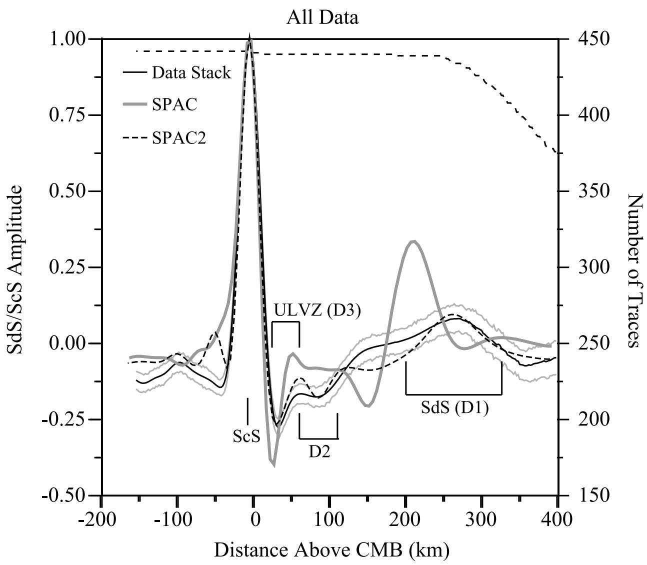

Figure 4. Double-array stack of the entire data set (442 traces) shown by the solid black line with 95% confidence intervals estimated through bootstrap resampling [*Revenaugh and Meyer*, 1997] indicated by the light gray lines, along with stacks for synthetics for models SPAC (heavy gray line) and SPAC2 (dashed line). The vertical scale indicates the stack amplitude found assuming reflection from each depth, relative to the *ScS* arrival from the CMB. The number of traces contributing to the stack at each depth is indicated by the dashed line across the top and the scale on the right. The data stack shows a broad positive feature (D_1) extending from 200 to 350 km above the CMB, and two negative features (D_2 and D_3) near the CMB.

[15] To produce a new average model for the region, we modeled the data stack in Figure 4 using a simple three constant velocity layer model, with a positive discontinuity at the top of D″ (D_1), a velocity decrease about 60 km above the CMB (D_2), and a relatively thick, ULVZ with an upper discontinuity (D_3) 34 km above the CMB. This model, SPAC2, is shown in Figure 1. The fit to the data stack is quite good for SPAC2 (Figure 4), in terms of amplitudes and apparent depths of the imaged reflections from D_1, D_2, and D_3. The velocity contrasts and depths of the discontinuities are likely to be biased by stacking of data with variable timing of reflections, but as a basic characterization of the localized V_s structure, SPAC2 is more realistic than model M1. We do note that the presence of the combined D_2 and D_3 reductions in velocity does mimic the negative velocity gradient in M1 (see Figure 1).

[16] To assess the effects of lateral variations, we divide our data set into nine nonoverlapping subregions, or data bins, based on the location of *ScS* reflection points beneath the central Pacific (Figure 2a). The bin dimensions are chosen such that data sampling of each bin remains adequate to yield stable stacks while isolating coherent arrivals in each stack. Stacks with more than 30 traces tend to be quite stable, whereas stacks with less than 15 traces can be significantly impacted by a single trace. Small changes in the bin boundaries can lead to emergence of double peaks which appear to be sensing peaks isolated in adjacent bins; this indicates rapid spatial variations in the wavefield. We stack and model the data in each bin to obtain first-order constraints on variations in the D″ discontinuity across our study region, recognizing that the Fresnel zones of our data are such that our binned data are sensing sub-Fresnel zone scale lengths of heterogeneity. The stability of the stacks was assessed by normalizing the amplitudes of the waveforms relative to the RMS amplitude of the full trace rather than the *ScS* peak amplitude, finding that this makes little difference for stacks involving more than a dozen waveforms. We present results here using the *ScS*-normalized traces. We model the individual bin data stacks by stacking synthetic seismograms having the same distance distribution as the data contributing to each bin. This is important as it allows for any distance dependence of *ScS* amplitudes relative to shallower reflections or triplications. Synthetics are deconvolved by a source wavelet and low-pass filtered in the same manner as for the data. The resulting filtered synthetic spike trains are aligned on *ScS* and the trace amplitudes are normalized using the *ScS* peak amplitudes.

[17] Ideally, our synthetics would be for a 3-D structure, iteratively improved by adjusting the velocity structure. However, such complete modeling is both computationally and practically difficult; the structure is inadequately sampled to perform a sensible 3-D modeling study. We instead develop insight into the structure by finding localized one-dimensional velocity models that match the data stacks for each of our bins, produced by perturbing the depth and strengths of the 3 discontinuities in the SPAC2 model. This is effectively the first step toward characterizing the 3-D structure; as 1-D structures can be laterally smoothed into a 3-D model guided by the ray path geometry. Because we are modeling wide-angle reflections, for which the *SH* reflection coefficient is dependent only on the rigidity contrast, we hold the density structure fixed to that of PREM. We assume constant velocity layers, as we have no resolution of gradients within the layers. We vary parameters over a range of discontinuity depths and velocity contrasts for each feature until the stack of synthetics for each bin matches the amplitude and timing of each of the 3 features within D″ (i.e., D_1, D_2, D_3) to the degree that they are manifested in each data stack. Our philosophy in modeling the local bins was to emphasize the features that show up in the average stack, even though in some bins there are intermittent additional arrivals or scattered energy between D_1 and D_2. Because the additional arrivals are not coherent over more than one bin we do not try to fit each stack perfectly, recognizing that lateral variations and the limitations of localized 1-D models preclude meaningful results for more detailed structure.

3. Modeling Results

[18] Figure 5 shows double-array stacks of data and synthetics for local 1-D models for each of the nine bins. The multiple-event observations contributing to each of several bins are shown in the auxiliary material. Differences in the features discerned in the individual traces from bin to bin are apparent in their data stacks. The goal of double array stacking is to detect coherent arrivals and to reduce noise levels relative to the individual traces. Noise arises from incomplete suppression of source complexity, receiver coda, near-source scattering, and deconvolution inaccuracy.

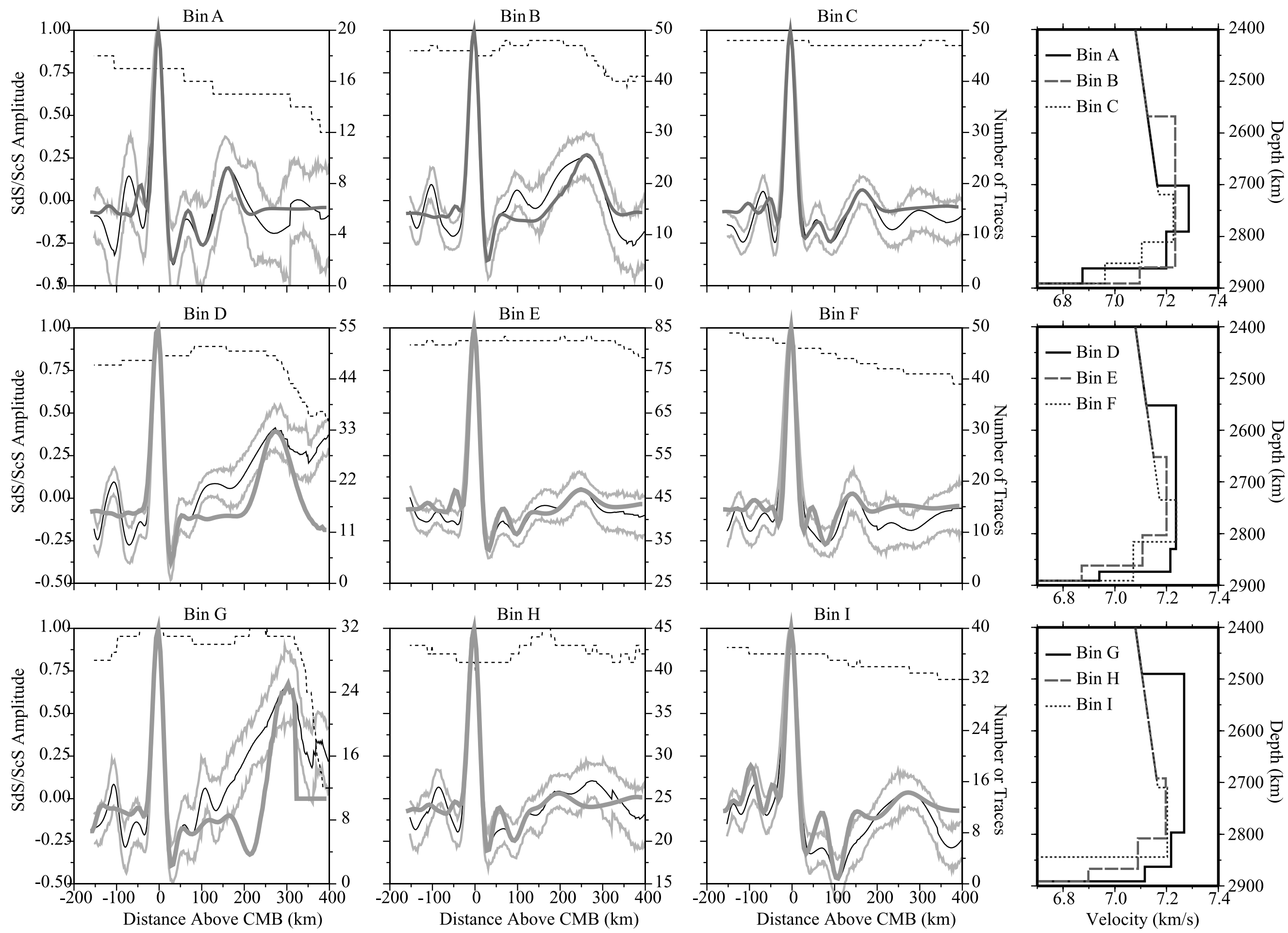

Figure 5. Data stacks (black lines) of binned subregions A through I (see Figure 2a for bin locations) with the stack for synthetics for a local 1-D model (medium gray) superimposed. Light gray lines denote the bounds of 95% confidence in the data stack. The dashed line in each stack corresponds to the number of traces contributing to the stack for each target depth. The model shear velocity V_s depth profiles are shown for each bin.

This will be most severe near the direct *S* phase, but also in the coda of *ScS*. Our modeling emphasizes the *ScS* precursor arrivals and extends only 400 km above the CMB to avoid direct *S* coda. We do not fit the post-*ScS* signal well, but this interval is strongly affected by receiver coda that we have not accounted for and which is enhanced by alignment of the traces on a strong arrival. One-dimensional synthetics predict multiple ULVZ reflections in this interval that are unlikely to exist in a laterally varying medium.

[19] Table 1 gives a summary of the modeling results, with Figure 6 plotting the solution parameters of the three-layer structures. Bins show variable stacks with positive D_1 (i.e., *SdS*) and negative D_2 and D_3 velocity jumps at widely ranging apparent depths relative to the CMB. It is important to recognize that the depths at which *SdS* energy is imaged directly depend upon the reference velocity model, M1. Reference models with higher average D″ velocities, such as PREM, decrease the apparent depth of the D_1 discontinuity and broaden the peak. About ±5 km variations in depth and ±0.2% velocity jump variations are admissible for any specific reference structure. However, synthetics do not reproduce all features in the data stack, thus larger reflector strength uncertainties actually exist. Small-scale D″ discontinuity (i.e., D_1) topography of about 100 km between some adjacent bins is suggested, but one must keep in mind the grazing geometry of the wavefield which suggests that the rapid variations are due to gradients in structure over larger scales.

[20] A west-to-east trend across the southernmost set of bins (G, H, and I) is very pronounced, as shown in Figures 5 and 6. Bin G has a very strong *SdS* peak (from D_1) near 300 km above the CMB. This weakens toward the east in Bins H and I. Arrivals from D_2 and D_3 (ULVZ) are seen in each of these bins, dramatically increasing in strength eastward. The model for Bin G includes a 2.3% D_1 discontinuity 401 km above the CMB. This is the strongest and shallowest discontinuity in our study area, comparable in strength to discontinuities seen under circum-Pacific regions at depths several hundred kilometers above the CMB. We do not detect any trend among the sources which would indicate that our systematic spatial variations result from a near-source effect, and the variation between events contributing to each bin further argues against such an explanation.

[21] *Russell et al.* [1999] document a strong southwest-to-northeast lateral gradient in *ScS-S* differential time anomalies, with progressively later *ScS* arrival times toward the

Table 1. Summary of Modeling Results

	Data Subset									
	Bin A	Bin B	Bin C	Bin D	Bin E	Bin F	Bin G	Bin H	Bin I	SPAC2[a]
D_1, km	2702	2568	2719	2552	2652	2735	2490	2692	2710	2632
V_0, km/s	7.164	7.127	7.169	7.122	7.150	7.174	7.105	7.162	7.167	7.145
V_1, km/s	7.286	7.234	7.226	7.236	7.200	7.238	7.268	7.197	7.202	7.202
$+dV_s^{0-1}$,%	1.7	1.5	0.8	1.6	0.7	0.9	2.3	0.5	0.5	0.8
D_2, km	2791	N/A	2811	2830	2803	2816	2797	2808	2844	2812
V_2, km/s	7.199	7.234	7.104	7.215	7.107	7.072	7.217	7.089	6.684	7.123
$-dV_s^{1-2}$,%	1.2	0	1.7	0.3	1.3	2.3	0.7	1.5	7.2	1.1
$-dV_s^{1-2}$ (with respect to PREM),%	0.9	N/A	2.2	0.7	2.2	2.7	0.7	2.4	8.0	2.0
D_3, km	2862	2860	2852	2874	2862	N/A	2863	2867	2880	2857
V_3, km/s	6.875	7.096	6.962	6.940	6.872	7.072	7.116	6.898	5.013	6.937
$-dV_s^{2-3}$,%	4.5	1.9	2.0	3.8	3.3	0	1.3	2.7	25.0	2.6
$-dV_s^{2-3}$ (with respect to PREM),%	4.5	2.3	4.2	4.5	5.4	N/A	2.0	5.1	31.0	4.5

[a]Results of modeling composite stack of all data.

northeast. This trend is contrary to the regional gradient from slow material in the southwest to faster material to the northeast in large-scale tomographic models, and is presumably a local feature not resolved by tomography, or a midmantle effect on *ScS* times. If the velocity within D″ decreases toward the northeast more than in either of our model space parameterizations, the effect would result in discontinuity depths in our models for the northeastern bins that are too high above the CMB. A strong northeastward increase in velocity within D″, as suggested by the trend in large-scale tomography models, could "flatten out" the reflector. However, this is contrary to the *ScS* anomalies of *Russell et al.* [1999], thus requiring structure elsewhere along the paths in the deep mantle. This is unlikely given the variation in source depth and location for events contributing to the trend. Overall, in contrast to the localized models of D″ structure beneath the Cocos Plate where a strong lateral gradient in velocity can account for variations in reflector strength for a discontinuity at uniform depth [*Lay et al.*, 2004a], the central Pacific data appear to favor large topography on the D″ (D_1) reflector, as well as significant topography (~20 km) on the deeper D_2 and D_3 reflectors, over lateral dimensions that allow our 130 km bin scales to sense the wavefield variations.

4. Discussion and Conclusion

[22] The strong lateral variation in *SdS* energy across the central Pacific study area appears to be more pronounced than observed in circum-Pacific regions when comparable spatial resolution (<500 km) is attained [e.g., *Reasoner and Revenaugh*, 1999; *Lay et al.*, 2004a; *Thomas et al.*, 2004]. More topography and a weaker velocity contrast for the D_1 reflector appear to be required under the central Pacific. The strong gradient in structure beneath the central Pacific provides a logical explanation for the variation in detection or characterization of the D″ discontinuity in prior work [e.g., *Garnero et al.*, 1988, 1993; *Kohler et al.*, 1997; *Sidorin et al.*, 1999a, 1999b; *Russell et al.*, 2001]. We also note that in this paper we have dubbed the deeper low-velocity layer (D_3) a ULVZ, but its shear velocity reductions are less than typically reported for ULVZ in other studies [e.g., see *Thorne and Garnero*, 2004].

[23] It is clear that no single average discontinuity model is representative of D″ structure in our study region, but there is consistency in the average of our models with the SPAC model of *Russell et al.* [2001]. The latter study used *S* wave data concentrated in our bins D, E, G and H. We find an average shear velocity increase of 1.3% for that subset of bins, at an average height above the CMB of 295 km, compared to the 1.7% increase 230 km above the CMB in model SPAC. *Reasoner and Revenaugh* [1999] detect variation in *PdP* amplitudes across 4 bins that overlap ours, with a southwest-to-northeast decrease in *PdP* amplitudes by a factor of 4, generally consistent with our *SdS* observations. It seems clear that toward the northeast of our study area both the *P* and *S* discontinuity structures are less pronounced.

[24] The observation of D″ discontinuities in high shear velocity regions beneath areas of present-day subduction has motivated interpretations involving subducted slab material, either separated crustal material that has piled up or actual slab thermal anomalies that have penetrated to the CMB [e.g., *Kendall and Silver*, 1996; *Wysession*, 1996; *Sidorin et al.*, 1999a, 1999b; *Garnero and Lay*, 2003]. The central Pacific, however, is far from any regions of recent subduction [*Bunge et al.*, 1998; *Lithgow-Bertelloni and Richards*, 1998], so it is difficult to make any connection to ongoing downwelling. While it is possible that an ancient rubble zone of material from subducted slabs is present under the central Pacific and has sufficient chemical contrast to produce intermittent reflections even long after thermal equilibration, this seems like an unlikely scenario given that the basic structure is not that different from circum-Pacific regions.

[25] The large-scale low shear velocity province present toward the southwest of our study area [*Mégnin and Romanowicz*, 2000; *Ritsema and van Heijst*, 2000; *Grand*, 2002] is generally associated with some form of rising superplume. However, it is unclear how such a structure can account for a shear velocity increase (D_1). The gradients in *ScS* traveltimes and *ScS-S* differential times [*Russell et al.*, 1999] across our study area suggest a southwest-to-northeast decrease in D″ shear velocity on a local scale. This can be reconciled with a relatively high-velocity layer (albeit low velocity relative to circum-Pacific regions overall) with a strong discontinuity in the southwest grading into a lower-velocity layer with a weak discontinuity in the northeast, essentially opposite to the

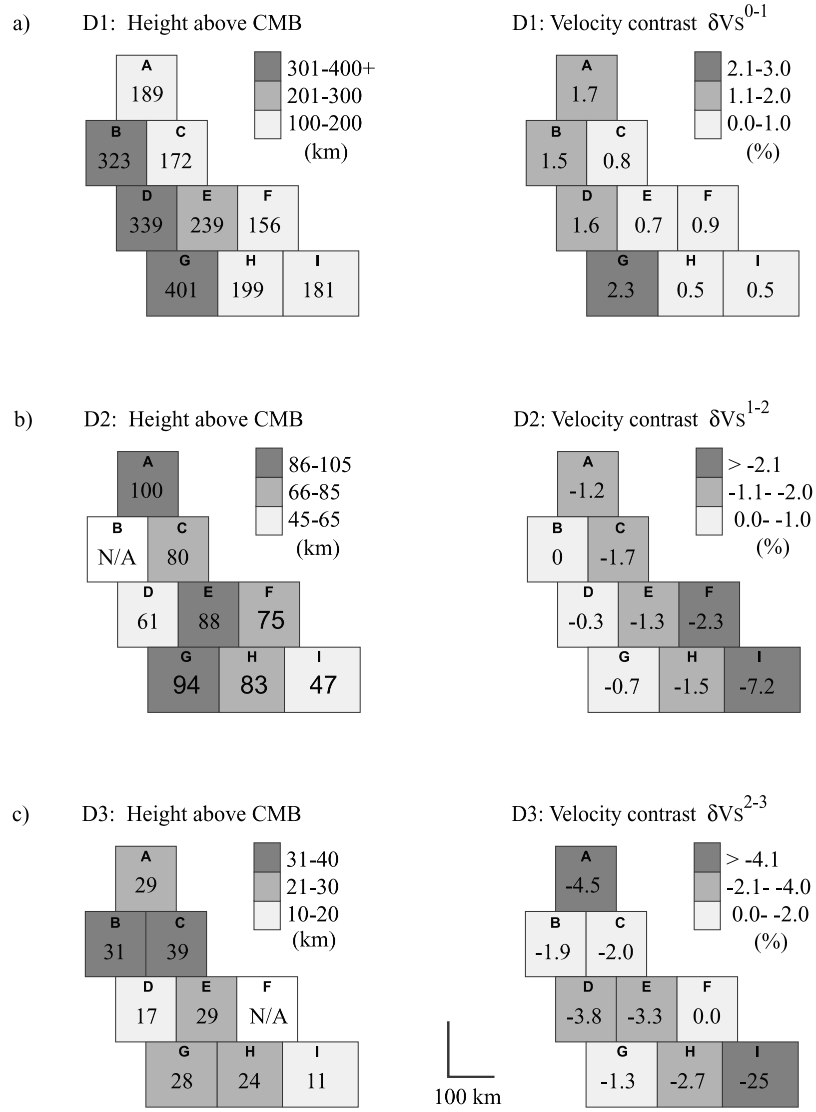

Figure 6. Summary of the modeled D_1, D_2, and D_3 reflector parameters (height above the CMB and% velocity contrast) for each bin. Shading provides a simplified visualization of relative values across the study region. This is not a rendition of a 3-D model; it is how grazing wave interaction with a more extensive 3-D structure is locally manifested.

trend inferred from large-scale tomography (see Figure 7). *Bréger et al.* [2001] do suggest the presence of very strong lateral gradients embedded within the overall transition from slow central Pacific to faster northern Pacific shear velocities in D″, so this is plausible. The strength of the lateral gradient in structure across our study area is comparable to that inferred from near vertically transiting waves in a region to the west [*Luo et al.*, 2001], and very strong lateral gradients in structure are observed on the margins of the low-velocity province in the deep mantle below Africa and the southern Atlantic/Indian Ocean [e.g., *Wen*, 2001; *Ni and Helmberger*, 2003; *Wang and Wen*, 2004; *Ni et al.*, 2005].

[26] Interpreting the D″ discontinuities as a phase change in a major mineral phase in the deep mantle has been proposed for some time [e.g., *Nataf and Houard*, 1993; *Sidorin et al.*, 1999b]. This possibility gained currency with the recent discovery of a phase transition of $MgSiO_3$ perovskite to postperovskite [*Murakami et al.*, 2004; *Iitaka et al.*, 2004; *Oganov and Ono*, 2004]. Unless disrupted by large chemical heterogeneities, one would expect such a phase change to be globally extensive, modulated in depth by thermal and minor chemical heterogeneities. *Sidorin et al.* [1999b] noted that the presence of D″ discontinuity structure under the central Pacific is pivotal for this hypothesis, and invoked estimated depths and velocity contrasts of the discontinuity to infer a positive Clapeyron slope of any phase change that may exist. Numerical calculations for the actual postperovskite phase do favor a large positive Clapeyron slope [*Tsuchiya et al.*, 2004a]. The proposed postperovskite transition is attractive as an explanation for the D″ discontinuity in that its elasticity favors stronger *S* velocity increases than for *P* velocity [e.g., *Tsuchiya et al.*, 2004b; *Stackhouse et al.*, 2005], as is generally observed.

[27] A large positive Clapeyron slope and the presence of a steep increase in temperature in the thermal boundary layer

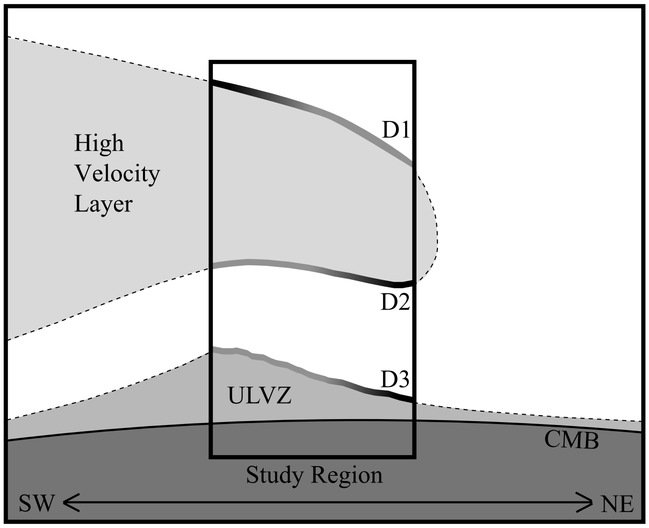

Figure 7. Schematic cross section of the imaged topography of the three reflectors, D_1, D_2, and D_3, as viewed from the southeast looking northwestward. The high-velocity layer (light gray), bounded by D_1 and D_2 reflectors, may involve the transition into (at D_1) and out of (at D_2) the postperovskite phase. The ULVZ (D_3, dark gray layer) thins and strengthens toward the east, possibly with an increase in melt component. The thick border lines within our study region (dark line) represent topography and strength of reflectors (darker means stronger reflections) directly constrained by our data. The thinner, dashed lines bordering layers outside our study region represent our inference of the structure sampled by the ray paths as they travel much further through the D″ region than the areal extent of our bins.

above the CMB could produce a 'double crossing' of the stability regime of postperovskite, with mantle rock transitioning back to the perovskite phase at greater depths within the D″ region [*Hernlund et al.*, 2005]. This possibility is especially intriguing in light of the negative D_2 feature modeled in this study, which is comparable in size to the velocity increase at D_1. *Flores and Lay* [2005] have demonstrated the difficulty of detecting precritical reflections from any velocity decreases within D″ compared to critical reflections from a velocity increase, arguing that stacking of carefully processed broadband data is essential for reliable detection. The current study achieves the level of signal-to-noise enhancement needed to identify the second phase boundary crossing, if that is what causes the D_2 feature.

[28] Figure 7 shows a schematic cross section of the imaged topography of our three imaged reflectors, D_1, D_2 and D_3, as viewed from the southeast looking northwestward. The high-velocity layer (light gray), bounded by D_1 and D_2 reflectors, can possibly be the transition into (at D_1) and out of (at D_2) the postperovskite phase, as advocated by *Hernlund et al.* [2005]. The weak ULVZ (D_3) thins and strengthens toward the east, possibly with an increasing melt component.

[29] The existence of the postperovskite phase transition also increases the likelihood that $MgSiO_3$ can account for some of the anisotropic properties of D″ [*Murakami et al.*, 2004], as the relatively smaller component of MgO had appeared more likely to account for observations than silicate perovskite [e.g., *McNamara et al.*, 2002; *Yamazaki and Karato*, 2002]. *Russell et al.* [1998, 1999] find evidence for lateral variations of *ScS* splitting across our study area, again with a southwest-to-northeast trend in the observations. The *ScS* splitting observations are rather bimodal, varying abruptly from *ScSH* fast in the southwest to *ScSV* fast in the northeast. This suggests that the southwestern region with a strong, relatively shallow D″ discontinuity and small *ScS-S* differential time anomalies has splitting with the fast wave being the *SH* component, while the northeastern region with either weak or no D″ discontinuity and large *ScS-S* differential time anomalies has splitting with the fast wave being the *SV* component. The correspondence between presence of the discontinuity and early *SH* arrivals is like that found in most circum-Pacific regions (see reviews by *Lay et al.* [1998] and *Moore et al.* [2004]), suggesting some causal linkage between the two phenomena.

[30] This study has attempted to characterize a heterogeneous medium using localized stacking and modeling approaches that only begin to resolve the 3-D heterogeneity. The data clearly exhibit rapid variations in the wavefield, but the variations do not necessarily arise from small-scale structure directly; grazing caustics and focusing/defocusing can cause amplitude fluctuations over small scales even if the responsible gradients are relatively much larger. Increasing the spatial resolution and using more flexible parameterizations to study D″ structure, such as migration approaches, is clearly important. Fully 3-D wavefield modeling is also needed, however, detailed 1-D models like those we have developed here are necessary to guide construction of 3-D structures used for advanced modeling techniques. Our future efforts in the central Pacific will be directed at scattering migrations and 3-D modeling of fine structure within the boundary layer, as this will be key to improving constraints on the nature of the D″ discontinuity in the region.

[31] **Acknowledgments.** Data were provided by the IRIS, BDSN, and TERRAscope/TRINET data centers. J. Polet provided helpful information about California station anisotropy corrections. We thank John Hernlund for discussions of interpretation of postperovskite structure. Justin Revenaugh and Colin Reasoner kindly made the double-array stacking and seismogram plotting software available. Justin Revenaugh, Michael Wysession, and anonymous reviewers provided helpful comments on the manuscript. This research was supported by NSF grant EAR0125595 (T.L.) and NSF grant EAR-0135119 (E.J.G.). Contribution 485 of the Center for the Study of Imaging and Dynamics of the Earth, IGPP, UCSC.

References

Bréger, L., and B. Romanowicz (1998), Three-dimensional structure at the base of the mantle beneath the central Pacific, *Science*, *282*, 718–720.

Bréger, L., B. Romanowicz, and C. Ng (2001), The Pacific plume as seen by *S*, *ScS*, and *SKS*, *Geophys. Res. Lett.*, *28*, 1859–1862.

Bunge, H.-P., M. A. Richards, C. Lithgow-Bertelloni, J. R. Baumgardner, S. P. Grand, and B. A. Romanowicz (1998), Time scales and heterogeneous structure in geodynamic Earth models, *Science*, *280*, 91–95.

Dziewonski, A. M., and D. L. Anderson (1981), Preliminary reference Earth model, *Phys. Earth Planet. Inter.*, *25*, 297–356.

Flores, C., and T. Lay (2005), The trouble with seeing double, *Geophys. Res. Lett.*, *32*, L24305, doi:10.1029/2005GL024366.

Ford, S. R., E. J. Garnero, and A. K. McNamara (2006), A strong lateral shear velocity gradient and anisotropy heterogeneity in the lowermost mantle beneath the southern Pacific, *J. Geophys. Res.*, *111*, B03306, doi:10.1029/2004JB003574.

Garnero, E. J., and D. V. Helmberger (1993), Travel times of *S* and *SKS*: Implications for three-dimensional lower mantle structure beneath the central Pacific, *J. Geophys. Res.*, *98*, 8225–8241.

Garnero, E. J., and T. Lay (2003), D″ shear velocity heterogeneity, anisotropy, and discontinuity structure beneath the Caribbean and Central America, *Phys. Earth Planet. Inter.*, *140*, 219–242.
Garnero, E. J., D. V. Helmberger, and G. Engen (1988), Lateral variations near the core-mantle boundary, *Geophys. Res. Lett.*, *15*, 609–612.
Garnero, E. J., D. V. Helmberger, and S. Grand (1993), Preliminary evidence for a lower mantle shear wave velocity discontinuity beneath the central Pacific, *Phys. Earth Planet. Inter.*, *79*, 335–347.
Grand, S. P. (2002), Mantle shear-wave tomography and the fate of subducted slabs, *Philos. Trans. R. Soc. London, Ser. A*, *360*, 2475–2491.
Hernlund, J. W., C. Thomas, and P. J. Tackley (2005), A doubling of the post-perovskite phase boundary and structure of the Earth's lowermost mantle, *Nature*, *434*, 882–886.
Iitaka, T., K. Hirose, K. Kawamura, and M. Murakami (2004), The elasticity of the $MgSiO_3$ post-perovskite phase in the Earth's lowermost mantle, *Nature*, *430*, 442–444.
Kendall, J.-M., and P. G. Silver (1996), Constraints from seismic anisotropy on the nature of the lowermost mantle, *Nature*, *381*, 409–412.
Kohler, M. D., J. E. Vidale, and P. M. Davis (1997), Complex scattering within D″ observed on the very dense Los Angeles Region Seismic Experiment passive array, *Geophys. Res. Lett.*, *24*, 1855–1858.
Lay, T., and E. J. Garnero (2004), Core-mantle boundary structures and processes, in *The State of the Planet: Frontiers and Challenges in Geophysics*, *Geophys. Monogr. Ser.*, vol. 150, edited by R. S. J. Sparks and C. J. Hawkesworth, 25–41, AGU, Washington, D. C.
Lay, T., and D. V. Helmberger (1983a), A lower mantle *S*-wave triplication and the shear velocity structure of D″, *Geophys. J. R. Astron. Soc.*, *75*, 799–838.
Lay, T., and D. V. Helmberger (1983b), The shear wave velocity gradient at the base of the mantle, *J. Geophys. Res.*, *88*, 8160–8170.
Lay, T., Q. Williams, E. J. Garnero, L. Kellogg, and M. E. Wysession (1998), Seismic wave anisotropy in the D″ region and its implications, in *The Core-Mantle Boundary Region*, edited by M. Gurnis et al., pp. 299–318, AGU, Washington, D. C.
Lay, T., E. J. Garnero, and S. A. Russell (2004a), Lateral variation of the D″ discontinuity beneath the Cocos plate, *Geophys. Res. Lett.*, *32*, L15612, doi:10.1029/2004GL020300.
Lay, T., E. J. Garnero, and Q. Williams (2004b), Partial melting in a thermo-chemical boundary layer at the base of the mantle, *Phys. Earth Planet. Inter.*, *146*, 441–467.
Lithgow-Bertelloni, C., and M. A. Richards (1998), The dynamics of Cenozoic and Mesozoic plate motions, *Rev. Geophys.*, *36*, 27–78.
Luo, S. N., S. D. Ni, and D. V. Helmberger (2001), Evidence for a sharp lateral variation of velocity at the core-mantle boundary from multipathed *PKPab*, *Earth Planet. Sci. Lett.*, *189*, 155–164.
Masters, G., G. Laske, H. Bolton, and A. M. Dziewonski (2000), The relative behavior of shear velocity, bulk sound speed, and compressional velocity in the mantle: Implications for chemical and thermal structure, in *Earth's Deep Interior: Mineral Physics and Tomography From the Atomic to the Global Scale*, edited by S. Karato et al., pp. 63–87, AGU, Washington, D. C.
McNamara, A. K., P. E. van Keken, and S.-I. Karato (2002), Development of anisotropic structure in the Earth's lower mantle by solid-state convection, *Nature*, *416*, 310–314.
Mégnin, C., and B. Romanowicz (2000), The three-dimensional shear velocity structure of the mantle from the inversion of body, surface and higher-mode waveforms, *Geophys. J. Int.*, *143*, 709–728.
Moore, M., E. J. Garnero, T. Lay, and Q. Williams (2004), Synthesizing shear wave splitting and waveform complexity for lowermost mantle structures with low-velocity lamellae and transverse isotropy, *J. Geophys. Res.*, *109*, B02319, doi:10.1029/2003JB002546.
Mori, J., and D. V. Helmberger (1995), Localized boundary layer below the mid-Pacific velocity anomaly identified from a *PcP* precursor, *J. Geophys. Res.*, *100*, 20,359–20,365.
Müller, G. (1985), The reflectivity method: A tutorial, *Z. Geophys.*, *58*, 153–174.
Murakami, M., K. Hirose, K. Kawamura, N. Sata, and Y. Ohishi (2004), Post-perovskite phase transition in $MgSiO_3$, *Science*, *304*, 855–858.
Nataf, H.-C., and S. Houard (1993), Seismic discontinuity at the top of D″: A world-wide feature?, *Geophys. Res. Lett.*, *20*, 2371–2374.
Ni, S., and D. V. Helmberger (2003), Ridge-like lower mantle structure beneath South Africa, *J. Geophys. Res.*, *108*(B2), 2094, doi:10.1029/2001JB001545.
Ni, S., D. V. Helmberger, and J. Tromp (2005), Three-dimensional structure of the Africa superplume from waveform modeling, *Geophys. J. Int.*, *161*, 283–294.
Oganov, A. R., and S. Ono (2004), Theoretical and experimental evidence for a post-perovskite phase of $MgSiO_3$ in Earth's D″ layer, *Nature*, *430*, 445–448.
Polet, J., and H. Kanamori (2002), Anisotropy beneath California: Shear wave splitting measurements using a dense broadband array, *Geophys. J. Int.*, *149*, 313–327.
Reasoner, C., and J. Revenaugh (1999), Short-period *P* wave constraints on D″ reflectivity, *J. Geophys. Res.*, *104*, 955–961.
Revenaugh, J., and R. Meyer (1997), Seismic evidence of partial melt within a possibly ubiquitous low-velocity layer at the base of the mantle, *Science*, *277*, 670–673.
Ritsema, J., and H.-J. van Heijst (2000), Seismic imaging of structural heterogeneity in Earth's mantle: Evidence for large-scale mantle flow, *Sci. Progress*, *83*, 243–259.
Ritsema, J., E. Garnero, and T. Lay (1997), A strongly negative shear velocity gradient and lateral variability in the lowermost mantle beneath the Pacific, *J. Geophys. Res.*, *102*, 20,395–20,411.
Russell, S. A., T. Lay, and E. J. Garnero (1998), Seismic evidence for small-scale dynamics in the lowermost mantle at the root of the Hawaiian hotspot, *Nature*, *396*, 255–258.
Russell, S. A., T. Lay, and E. J. Garnero (1999), Small-scale lateral shear velocity and anisotropy heterogeneity near the core-mantle boundary beneath the central Pacific imaged using broadband *ScS* waves, *J. Geophys. Res.*, *104*, 13,183–13,199.
Russell, S. A., C. Reasoner, T. Lay, and J. Revenaugh (2001), Coexisting shear- and compressional-wave seismic velocity discontinuities beneath the central Pacific, *Geophys. Res. Lett.*, *28*, 2281–2284.
Schlittenhardt, J., J. Schweitzer, and G. Müller (1985), Evidence against a discontinuity at the top of D″, *Geophys. J. R. Astron. Soc.*, *81*, 295–306.
Sidorin, I., M. Gurnis, and D. V. Helmberger (1999a), Evidence for a ubiquitous seismic discontinuity at the base of the mantle, *Science*, *286*, 1326–1331.
Sidorin, I., M. Gurnis, and D. V. Helmberger (1999b), Dynamics of a phase change at the base of the mantle consistent with seismological observations, *J. Geophys. Res.*, *104*, 15,005–15,023.
Silver, P. G. (1996), Seismic anisotropy beneath the continents: Probing the depths of geology, *Annu. Rev. Earth Planet. Sci.*, *24*, 385–432.
Stackhouse, S., J. P. Brodholt, G. D. Price, J. Wookey, and J. M. Kendall (2005), The effect of temperature on the acoustic anisotropy of the perovskite and post-perovskite polymorphs of $MgSiO_3$, *Earth Planet. Sci. Lett.*, *230*, 1–10.
Thomas, C., E. J. Garnero, and T. Lay (2004), High-resolution image of lowermost mantle structure under the Cocos Plate, *J. Geophys. Res.*, *109*, B08307, doi:10.1029/2004JB003013.
Thorne, M. S., and E. J. Garnero (2004), Inferences on ultralow-velocity structure from a global analysis of *SPdKS* waves, *J. Geophys. Res.*, *109*, B08301, doi:10.1029/2004JB003010.
To, A., B. Romanowicz, Y. Capdeville, and N. Takeuchi (2005), 3D effects of sharp boundaries at the borders of the African and Pacific superplumes: Observation and modeling, *Earth Planet. Sci. Lett.*, *233*, 137–153.
Tsuchiya, T., J. Tsuchiya, K. Umemoto, and R. M. Wentzcovitch (2004a), Phase transition in $MgSiO_3$ perovskite in the Earth's lower mantle, *Earth Planet. Sci. Lett.*, *224*, 241–248.
Tsuchiya, T., J. Tsuchiya, K. Umemoto, and R. M. Wentzcovitch (2004b), Elasticity of post-perovskite $MgSiO_3$, *Geophys. Res. Lett.*, *31*, L14603, doi:10.1029/2004GL020278.
Wang, Y., and L. Wen (2004), Mapping the geometry and geographic distribution of a very low velocity province at the base of the Earth's mantle, *J. Geophys. Res.*, *109*, B10305, doi:10.1029/2003JB002674.
Wen, L. (2001), Seismic evidence for a rapidly-varying compositional anomaly at the base of the Earth's mantle beneath Indian Ocean, *Earth Planet. Sci. Lett.*, *194*, 83–95.
Wysession, M. E. (1996), Imaging cold rock at the base of the mantle: The sometimes fate of Slabs?, in *Subduction: Top to Bottom*, edited by G. E. Bebout et al., pp. 369–384, AGU, Washington, D. C.
Wysession, M. E., T. Lay, J. Revenaugh, Q. Williams, E. J. Garnero, R. Jeanloz, and L. H. Kellogg (1998), The D″ discontinuity and its implications, in *The Core-Mantle Boundary Region*, edited by M. Gurnis et al., pp. 273–297, AGU, Washington, D. C.
Yamazaki, D., and S.-I. Karato (2002), Fabric development in (MgO) during large strain shear deformation: Implications for seismic anisotropy in Earth's lower mantle, *Phys. Earth Planet. Inter.*, *131*, 251–267.

M. Avants and T. Lay, Earth Sciences Department, University of California, 1156 High Street, Santa Cruz, CA 95064, USA. (thorne@pmc.ucsc.edu)

E. J. Garnero, Department of Geological Sciences, Arizona State University, Box 871404, Tempe, AZ 85287-1404, USA.

S. A. Russell Gonzalez, Marston Science Library, University of Florida, P.O. Box 117011, Gainesville, FL 32611-7011, USA.